

Manuscript version: Published Version

The version presented in WRAP is the published version (Version of Record).

Persistent WRAP URL:

<http://wrap.warwick.ac.uk/166833>

How to cite:

Please refer to published version for the most recent bibliographic citation information. If a published version is known of, the repository item page linked to above, will contain details on accessing it.

Copyright and reuse:

The Warwick Research Archive Portal (WRAP) makes this work by researchers of the University of Warwick available open access under the following conditions.

Copyright © and all moral rights to the version of the paper presented here belong to the individual author(s) and/or other copyright owners. To the extent reasonable and practicable the material made available in WRAP has been checked for eligibility before being made available.

Copies of full items can be used for personal research or study, educational, or not-for-profit purposes without prior permission or charge. Provided that the authors, title and full bibliographic details are credited, a hyperlink and/or URL is given for the original metadata page and the content is not changed in any way.

Publisher's statement:

Please refer to the repository item page, publisher's statement section, for further information.

For more information, please contact the WRAP Team at: wrap@warwick.ac.uk.

Tomographic entanglement indicators from NMR experiments

Cite as: *J. Chem. Phys.* **156**, 154102 (2022); doi: [10.1063/5.0087032](https://doi.org/10.1063/5.0087032)

Submitted: 31 January 2022 • Accepted: 28 March 2022 •

Published Online: 18 April 2022



View Online



Export Citation



CrossMark

B. Sharmila,^{1,a),b)}  V. R. Krithika,^{2,3} Soham Pal,^{2,3} T. S. Mahesh,^{2,3} S. Lakshmibala,¹ and V. Balakrishnan¹ 

AFFILIATIONS

¹Department of Physics, Indian Institute of Technology Madras, Chennai 600036, India

²Department of Physics, Indian Institute of Science Education and Research, Pune 411008, India

³NMR Research Center, Indian Institute of Science Education and Research, Pune 411008, India

^{a)}Author to whom correspondence should be addressed: Sharmila.Balamurugan@warwick.ac.uk

^{b)}Present address: Department of Physics, University of Warwick, Coventry CV4 7AL, United Kingdom.

ABSTRACT

In recent years, the performance of different entanglement indicators obtained directly from tomograms has been assessed in continuous-variable and hybrid quantum systems. In this paper, we carry out this task in the case of spin systems. We compute the entanglement indicators from actual experimental data obtained from three liquid-state nuclear magnetic resonance (NMR) experiments and compare them with standard entanglement measures calculated from the corresponding density matrices, both experimentally reconstructed and numerically computed. The gross features of entanglement dynamics and spin squeezing properties are found to be reproduced by these entanglement indicators. However, the extent to which these indicators and spin squeezing track the entanglement during time evolution of the multipartite systems in the NMR experiments is very sensitive to the precise nature and strength of interactions as well as the manner in which the full system is partitioned into subsystems. We also use the IBM quantum computer to implement equivalent circuits that capture the dynamics of the multipartite system in one of the NMR experiments and carry out a similar comparative assessment of the performance of tomographic indicators. This exercise shows that these indicators can estimate the degree of entanglement without necessitating detailed state reconstruction procedures, establishing the advantage of the tomographic approach.

Published under an exclusive license by AIP Publishing. <https://doi.org/10.1063/5.0087032>

I. INTRODUCTION

Manipulating nuclear spins in small molecules in liquids using nuclear magnetic resonance (NMR) techniques has led to successful demonstrations of quantum information processing (QIP),^{1,2} owing to the intrinsic quantum nature of the electronic, nuclear, and spin degrees of freedom in molecules.^{2–5} The experimental realization of quantum teleportation⁶ using ESR and multiparty quantum clock synchronization⁷ using NMR has been reported recently. NMR techniques⁸ have also demonstrated spin-squeezing^{9,10} and the generation¹¹ and estimation^{12,13} of entanglement. Nuclear spins thus furnish an ideal platform for the study of quantum correlations.

As QIP relies heavily on entanglement, estimating the extent of entanglement is of great importance. The computation of most commonly used entanglement measures entails prior knowledge of the density matrix (of the full system), which is not directly accessible to experimental measurements. The outcome of measurements

of a physical quantity in a quantum system is essentially a histogram of the state of the system in terms of the basis states corresponding to the observable concerned. A tomogram comprises a set of such histograms, obtained by measurements of an informationally complete quorum of observables. The deduction of the density matrix of the system from tomograms is the primary objective of quantum state reconstruction. NMR techniques have been used^{14–16} to investigate quantum state tomography and reconstruction in nuclear spin systems. However, state reconstruction from tomograms is not error-free, as it entails statistical methods.¹⁷ If the tomographic slices considered contain a significant amount of experimental noise, the inverse transformation performed to carry out state reconstruction is known to lead to features in the reconstructed state that are not present in the original.^{18,19} This drawback is present even in as simple a situation as a 2-qubit bipartite system and is naturally more pronounced when there is multipartite entanglement.²⁰ Several difficulties arise^{21,22} in developing scalable reconstruction procedures

when large numbers of qubits are involved. Standard reconstruction procedures in such cases require large sets of positive-operator-valued measurements and are very time consuming. Other procedures involving compressed sensing^{23–26} have been suggested to characterize an unknown quantum state using only a subset of the data. While specific entangled multiqubit pure states with special features in the density matrix have been reconstructed reasonably well, reconstruction of an arbitrary multiqubit state, in general, still poses serious challenges.

It is necessary, therefore, to extract as much information about a quantum state as possible directly from tomograms, circumventing state reconstruction. This may be done²⁷ in bipartite qubit systems by using the tomogram to compute the fidelity of the state with respect to some specific target states. Of special interest is the estimation of entanglement from easily carried out operations on the tomograms concerned. This has been done in the case of continuous-variable (CV) systems involving a radiation field, illustrating the usefulness of this approach. For instance, the entanglement between the radiation fields in the output ports of a quantum beamsplitter has been identified qualitatively from tomograms.²⁸ Further, a quantitative analysis of entanglement using several indicators based directly on tomograms in bipartite CV and multipartite hybrid quantum (HQ) systems has been carried out,^{29,30} and the results have been compared with standard entanglement measures such as the quantum mutual information.

This paper presents such a comparison for nuclear spin systems. The exercise is important in understanding the usefulness of tomographic entanglement indicators in the broad framework comprising CV, spin, and HQ systems. A major difference from earlier work is that the investigations reported here are based on the actual data from three different liquid-state NMR experiments (labeled I, II, and III in the sequel), rather than data from numerically generated states. The details regarding the methods of state preparation, the data obtained, and the errors involved in the experiments have been reported elsewhere.^{31,32} Experiments I and III have been performed on ¹³C, ¹H, and ¹⁹F spin-half nuclei in dibromofluoromethane (DBFM) dissolved in deuterated acetone.³¹ NMR experiment II has been performed on ¹⁹F and ³¹P spin-half nuclei in sodium fluorophosphate (NaFP) dissolved in D₂O.³² We have also addressed the problem of identifying the optimal number of measurements (equivalently, the number of tomographic slices) needed to obtain good entanglement indicators.

The plan of this paper is as follows: In Sec. II, we define spin tomograms, recapitulate their salient features, and introduce the tomographic entanglement indicators. In Sec. III, we list the conventional measures of entanglement that are used subsequently to benchmark the performance of our indicators. In Sec. IV, we briefly review the procedure for obtaining squeezing properties both from the tomograms directly and from the state. In Sec. V, tomograms corresponding to NMR experiment I are analyzed. We also comment on the spin, higher-order, and entropic squeezing properties of this system as deduced from tomograms. In Sec. VI, we examine NMR experiments II and III, and analyze the squeezing properties and the entanglement indicators obtained directly from relevant tomograms. The three NMR experiments considered here are on either bipartite or tripartite spin systems, and bipartite entanglement has been investigated in all cases. In the Appendix, we have proposed equivalent circuits for NMR experiment I at specific instants

of time and implemented them in the IBM quantum computing platform (IBM Q). Corresponding tomograms have been obtained both from the experimental runs in the IBM Q platform and from numerical simulations using the IBM open quantum assembly language (QASM) simulator.^{33,34} The idea behind using the IBM platform is twofold: (i) to implement an equivalent circuit that models the dynamics in the system of interest and (ii) to demonstrate that the extent of entanglement can be assessed in this equivalent setup without resorting to detailed state reconstruction.

II. SPIN TOMOGRAMS

A. Notation and definitions

The quorum of observables³⁵ for a single spin- $\frac{1}{2}$ system is given by

$$\begin{aligned}\sigma_x &= \frac{1}{2}(|\uparrow\rangle\langle\downarrow| + |\downarrow\rangle\langle\uparrow|), & \sigma_y &= \frac{i}{2}(|\downarrow\rangle\langle\uparrow| - |\uparrow\rangle\langle\downarrow|), \\ \sigma_z &= \frac{1}{2}(|\uparrow\rangle\langle\uparrow| - |\downarrow\rangle\langle\downarrow|).\end{aligned}\quad (1)$$

$|\downarrow\rangle$ and $|\uparrow\rangle$ stand for the eigenstates of σ_z , as usual. For notational convenience in this section, we denote $|\downarrow\rangle$ and $|\uparrow\rangle$ by $|-\frac{1}{2}\rangle$ and $|+\frac{1}{2}\rangle$, respectively, so that $\sigma_z|m\rangle = m|m\rangle$, where $m = \pm 1/2$. The state $|\vartheta, \varphi, m\rangle = U(\vartheta, \varphi)|m\rangle$, where

$$U(\vartheta, \varphi) = \begin{bmatrix} \cos\left(\frac{\vartheta}{2}\right)e^{i\varphi/2} & \sin\left(\frac{\vartheta}{2}\right)e^{i\varphi/2} \\ -\sin\left(\frac{\vartheta}{2}\right)e^{-i\varphi/2} & \cos\left(\frac{\vartheta}{2}\right)e^{-i\varphi/2} \end{bmatrix}.$$

Using the unit vector \mathbf{n} to denote the direction specified by (ϑ, φ) , the qubit tomogram is given by

$$w(\mathbf{n}, m) = \langle \mathbf{n}, m | \rho_S | \mathbf{n}, m \rangle, \quad (2)$$

where ρ_S is the qubit density matrix. There exists a basis for each value of \mathbf{n} so that $\sum_m w(\mathbf{n}, m) = 1$.

It is straightforward to extend the foregoing to multipartite spin systems. For a bipartite system, in particular, the quorum is the set of nine direct product combinations of the operators defined in Eq. (1). The bipartite tomogram

$$w(\mathbf{n}_A, m_A; \mathbf{n}_B, m_B) = \langle \mathbf{n}_A, m_A; \mathbf{n}_B, m_B | \rho_{AB} | \mathbf{n}_A, m_A; \mathbf{n}_B, m_B \rangle, \quad (3)$$

where ρ_{AB} is the bipartite density matrix, $\sigma_{iz}|m_i\rangle = m_i|m_i\rangle$ ($i = A, B$), and $|\mathbf{n}_A, m_A; \mathbf{n}_B, m_B\rangle$ stands for $|\mathbf{n}_A, m_A\rangle \otimes |\mathbf{n}_B, m_B\rangle$. The normalization condition is given by

$$\sum_{m_A, m_B} w(\mathbf{n}_A, m_A; \mathbf{n}_B, m_B) = 1 \quad (4)$$

for each \mathbf{n}_A and \mathbf{n}_B . The reduced tomograms for the subsystems A and B are

$$w_A(\mathbf{n}_A, m_A) = \langle \mathbf{n}_A, m_A | \rho_A | \mathbf{n}_A, m_A \rangle = \sum_{m_B} w(\mathbf{n}_A, m_A; \mathbf{n}_B, m_B) \quad (5)$$

for any fixed value of \mathbf{n}_B and

$$w_B(\mathbf{n}_B, m_B) = \langle \mathbf{n}_B, m_B | \rho_B | \mathbf{n}_B, m_B \rangle = \sum_{m_A} w(\mathbf{n}_A, m_A; \mathbf{n}_B, m_B) \quad (6)$$

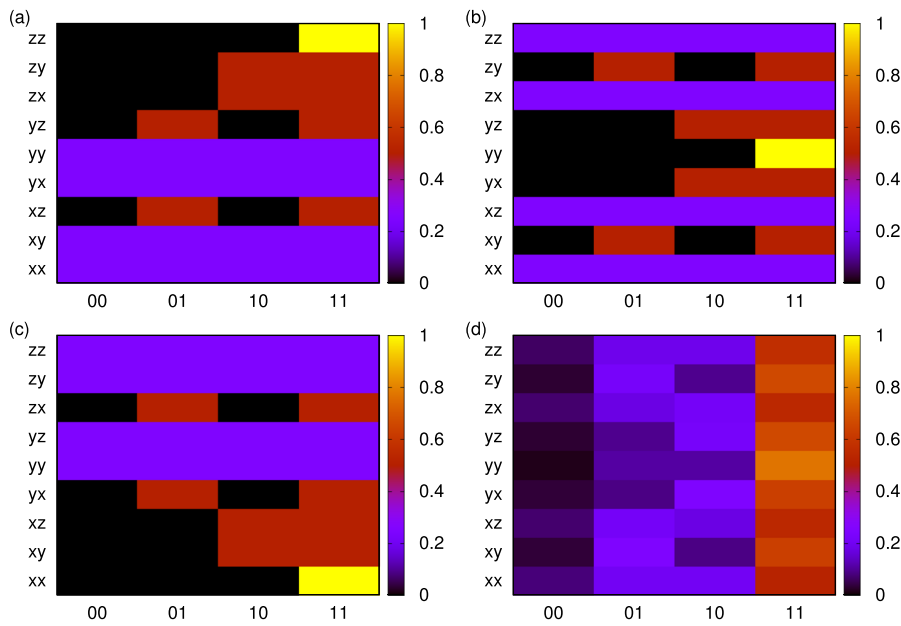


FIG. 1. Tomograms of spin coherent states with (θ, ϕ) equal to (a) $(0, 0)$, (b) $(\pi/2, \pi/2)$, (c) $(\pi/2, 0)$, and (d) $(\pi/3, \pi/3)$. The bases are denoted by $x, y,$ and z and the outcomes by 0 and 1.

for any fixed value of \mathbf{n}_A . The reduced density matrices ρ_A and ρ_B are given by $\text{Tr}_B(\rho_{AB})$ and $\text{Tr}_A(\rho_{AB})$.

It is convenient to plot bipartite spin tomograms in the form of color maps. On the vertical axis, we mark the nine possibilities $xx, xy,$ etc., in which the first and second labels correspond to subsystems A and B, respectively. Each basis has four outcomes, namely, 00, 01, 10, and 11 where 0 and 1 refer to $m = -1/2$ and $m = +1/2$, respectively. Hence, each color map is essentially a representation of a (9×4) matrix. As a specific example, we present the spin tomograms for a bipartite spin coherent state parameterized by angles θ, ϕ (where $0 \leq \theta \leq \pi, 0 \leq \phi < 2\pi$), given by

$$\begin{aligned} & \left[\cos(\theta/2)|\uparrow\rangle_A + e^{i\phi} \sin(\theta/2)|\downarrow\rangle_A \right] \\ & \otimes \left[\cos(\theta/2)|\uparrow\rangle_B + e^{i\phi} \sin(\theta/2)|\downarrow\rangle_B \right]. \end{aligned} \quad (7)$$

Figures 1(a)–1(d) show the tomograms for four different values of θ and ϕ .

B. Tomographic entanglement indicators

We use tomographic entropies to estimate the degree of correlation between the subsystems. The bipartite tomographic entropy is given by

$$S(\mathbf{n}_A, \mathbf{n}_B) = - \sum_{m_A, m_B} w(\mathbf{n}_A, m_A; \mathbf{n}_B, m_B) \log_2 w(\mathbf{n}_A, m_A; \mathbf{n}_B, m_B). \quad (8)$$

For a given subsystem, the tomographic entropy is

$$S(\mathbf{n}_i) = - \sum_{m_i} w_i(\mathbf{n}_i, m_i) \log_2 [w_i(\mathbf{n}_i, m_i)] \quad (i = A, B). \quad (9)$$

Some of the correlators to be defined are obtained from a section of the tomogram corresponding to specific values of \mathbf{n}_A and \mathbf{n}_B . The degree to which such a correlator is a satisfactory estimator

of entanglement, therefore, depends on the specific tomographic section involved. The correlators and the associated entanglement indicators are defined as follows.

The first of the tomographic entanglement indicators we consider is the mutual information $\varepsilon_{\text{TEI}}(\mathbf{n}_A, \mathbf{n}_B)$, expressed in terms of the tomographic entropies as

$$\varepsilon_{\text{TEI}}(\mathbf{n}_A, \mathbf{n}_B) = S(\mathbf{n}_A) + S(\mathbf{n}_B) - S(\mathbf{n}_A, \mathbf{n}_B). \quad (10)$$

Indicators based on the inverse participation ratio (IPR) are also found to be satisfactory estimators of entanglement.^{29,36} The participation ratio is a measure of delocalization in a given basis. The IPR corresponding to a bipartite system in the basis of the spin operators is defined as

$$\eta_{AB}(\mathbf{n}_A, \mathbf{n}_B) = \sum_{m_A} \sum_{m_B} [w(\mathbf{n}_A, m_A; \mathbf{n}_B, m_B)]^2. \quad (11)$$

The IPR for each subsystem is

$$\eta_i(\mathbf{n}_i) = \sum_{m_i} [w_i(\mathbf{n}_i, m_i)]^2 \quad (i = A, B). \quad (12)$$

The associated entanglement indicator is given by

$$\varepsilon_{\text{IPR}}(\mathbf{n}_A, \mathbf{n}_B) = 1 + \eta_{AB}(\mathbf{n}_A, \mathbf{n}_B) - \eta_A(\mathbf{n}_A) - \eta_B(\mathbf{n}_B). \quad (13)$$

Apart from $\varepsilon_{\text{TEI}}(\mathbf{n}_A, \mathbf{n}_B)$ and $\varepsilon_{\text{IPR}}(\mathbf{n}_A, \mathbf{n}_B)$, we have examined two other correlators that are familiar in the context of classical tomograms. Given two random variables X and Y , their Pearson correlation coefficient is defined as³⁷

$$\text{PCC}(X, Y) = \frac{\text{Cov}(X, Y)}{(\Delta X)(\Delta Y)}, \quad (14)$$

where ΔX and ΔY are the standard deviations of X and Y and $\text{Cov}(X, Y)$ is their covariance. In the present context, the correlation coefficient $\text{PCC}(m_A, m_B)$ calculated for fixed values of \mathbf{n}_A and

\mathbf{n}_B is relevant. A simple definition of the entanglement indicator is then

$$\varepsilon_{\text{PCC}}(\mathbf{n}_A, \mathbf{n}_B) = |\text{PCC}(m_A, m_B)|. \quad (15)$$

The modulus ensures that the quantifier of entanglement is non-negative. It is to be noted that $\text{PCC}(m_A m_B)$ has an implicit dependence on the directions \mathbf{n}_A and \mathbf{n}_B chosen, and that $\varepsilon_{\text{PCC}}(\mathbf{n}_A, \mathbf{n}_B)$ captures the effect of linear correlations.

The second indicator ε_{BD} that we shall use originates as follows: consider two discrete random variables X and Y , with a joint probability distribution $p_{XY}(x_i, y_j)$ and marginal distributions $p_X(x_i) = \sum_j p_{XY}(x_i, y_j)$ and $p_Y(y_j) = \sum_i p_{XY}(x_i, y_j)$. Their mutual information is the Kullback–Leibler divergence,^{38–40}

$$D_{\text{KL}}[p_{XY}:p_X p_Y] = \sum_{ij} p_{XY}(x_i, y_j) \log_2 \frac{p_{XY}(x_i, y_j)}{p_X(x_i) p_Y(y_j)}. \quad (16)$$

The indicator $\varepsilon_{\text{TEI}}(\mathbf{n}_A, \mathbf{n}_B)$ defined in Eq. (10) is just the mutual information in the case of spin tomograms, i.e.,

$$\varepsilon_{\text{TEI}}(\mathbf{n}_A, \mathbf{n}_B) = D_{\text{KL}}[w(\mathbf{n}_A, m_A; \mathbf{n}_B, m_B):w_A(\mathbf{n}_A, m_A)w_B(\mathbf{n}_B, m_B)]. \quad (17)$$

A simpler alternative to the Kullback–Leibler divergence is the Bhattacharyya distance,⁴¹

$$D_B[p_{XY}:p_X p_Y] = -\log_2 \left\{ \sum_{ij} [p_{XY}(x_i, y_j) p_X(x_i) p_Y(y_j)]^{1/2} \right\}. \quad (18)$$

An application of Jensen’s inequality leads to the bound $D_B \leq \frac{1}{2} D_{\text{KL}}$ so that D_B is an approximate (under-)estimate of the mutual information. It is thus natural to define, in analogy with Eq. (17), the entanglement indicator,

$$\varepsilon_{\text{BD}}(\mathbf{n}_A, \mathbf{n}_B) = D_B[w(\mathbf{n}_A, m_A; \mathbf{n}_B, m_B):w_A(\mathbf{n}_A, m_A)w_B(\mathbf{n}_B, m_B)]. \quad (19)$$

We may further remove the dependence on $(\mathbf{n}_A, \mathbf{n}_B)$ of the indicators defined above, by averaging over the nine possible values corresponding to the three orthogonal vectors for each of the \mathbf{n}_i ($i = A, B$). The average values of ε_{TEI} , ε_{IPR} , ε_{PCC} , and ε_{BD} thus obtained will be denoted by ξ_{TEI} , ξ_{IPR} , ξ_{PCC} , and ξ_{BD} , respectively.

III. ENTANGLEMENT MEASURES

In order to assess the efficacy of the tomographic indicators described in Sec. II B, we compare them with standard measures of entanglement. Such a basic measure of the entanglement between the two subsystems A and B of a bipartite system AB is the subsystem von Neumann entropy (SVNE) $\xi_{\text{SVNE}} = -\text{Tr}(\rho_i \log_2 \rho_i)$, where ρ_i ($i = A, B$) is the reduced (or subsystem) density matrix. When A and B are subsystems of a multipartite system, the mutual information

$$\xi_{\text{QMI}} = \xi_{\text{SVNE}}^{(A)} + \xi_{\text{SVNE}}^{(B)} - \xi_{\text{SVNE}}^{(AB)} \quad (20)$$

is a convenient measure of the correlations between A and B. Another standard measure of quantum correlations is provided by the quantum discord $D(B:A)$ between the two subsystems A and

B. If projective measurements are carried out on A, this discord is defined as

$$D(B:A) = \xi_{\text{SVNE}}^{(A)} - \xi_{\text{SVNE}}^{(AB)} + \min_{\{\mathcal{O}_i^A\}} \left\{ -\sum_j p_{ij}^A \text{Tr}(\mathcal{O}_{ij} \log_2 \mathcal{O}_{ij}) \right\}, \quad (21)$$

where $\{\mathcal{O}_i^A\}$ is a set of subsystem observables pertaining to A. Here,

$$p_{ij}^A = \text{Tr}[(\Pi_{ij}^A \otimes \mathbb{I}_B) \rho_{AB}] \quad (22)$$

and

$$\mathcal{O}_{ij} = \frac{\text{Tr}_A[(\Pi_{ij}^A \otimes \mathbb{I}_B) \rho_{AB} (\Pi_{ij}^A \otimes \mathbb{I}_B)]}{p_{ij}^A}, \quad (23)$$

where $\{\Pi_{ij}^A\}$ is the set of projection operators corresponding to \mathcal{O}_i^A and \mathbb{I}_B denotes the identity operator in B. $D(A:B)$ is similarly defined when projective measurements are carried out on B. In general, $D(A:B) \neq D(B:A)$.

IV. SQUEEZING PROPERTIES

In generic multipartite spin systems in which the subsystem states are entangled, spin squeezing is related to the entanglement.⁴² Bearing this in mind, we assess the squeezing properties of the NMR experiments I, II, and III via two different procedures. The first procedure is outlined in Ref. 43. The second method deduces squeezing properties directly from the corresponding spin tomograms. We have verified that the results obtained by two procedures are in agreement with each other, showing the usefulness of tomograms in extracting squeezing properties.

We first summarize the salient features of the procedure used in Ref. 43. This relies on the fact that the state of a system consisting of N spin- $\frac{1}{2}$ subsystems is squeezed if one of the components normal to the mean spin vector of the system has a variance less than $N/4$, which is the variance of the corresponding spin coherent state. For instance, if $N = 2$, the mean spin direction is given by $\mathbf{v}_s(t) = \langle \mathbf{J}_2(t) \rangle / |\langle \mathbf{J}_2(t) \rangle|$, where

$$\mathbf{J}_2 = (\sigma_{Ax} + \sigma_{Bx})\mathbf{e}_x + (\sigma_{Ay} + \sigma_{By})\mathbf{e}_y + (\sigma_{Az} + \sigma_{Bz})\mathbf{e}_z. \quad (24)$$

Here, $\langle \mathcal{O}(t) \rangle = \text{Tr}_{\text{AB}}(\rho_{\text{AB}}(t)\mathcal{O})$ for any operator \mathcal{O} , where $\rho_{\text{AB}}(t)$ is the density matrix at time t . As a first step, the variance

$$(\Delta \mathbf{J}_2 \cdot \mathbf{v}_\perp)^2 = \langle (\mathbf{J}_2 \cdot \mathbf{v}_\perp)^2 \rangle \quad (25)$$

is calculated as a function of t for several different vectors \mathbf{v}_\perp , which satisfy $\mathbf{v}_\perp \cdot \mathbf{v}_s = 0$ at each instant. The next step is to identify the minimum variance $(\Delta J_{\text{min}})^2$ at each instant. From this, the quantity $[1 - 2(\Delta J_{\text{min}})^2]$ computed at various instants yields the degree of squeezing as a function of time.

Alternatively, we may assess the spin squeezing properties solely from tomograms. In order to compute variances from any generic spin tomogram, we need to express $(\Delta \mathbf{J}_2 \cdot \mathbf{v}_\perp)^2$ in terms of quantities that are readily obtained from the relevant tomogram. Using the commutators of the spin operators, it is easy to see that this is possible: $(\mathbf{J}_2 \cdot \mathbf{v}_\perp)^2$ involves either terms linear in the σ 's, such as σ_{Ax} , or products of σ 's, such as $\sigma_{Ax}\sigma_{By}$.

The expectation values of these operators are readily found. For instance, $\langle \sigma_{Ax} \rangle = \sum_{m_A, m_B} m_A w(\mathbf{e}_x, m_A; \mathbf{e}_y, m_B)$, while $\langle \sigma_{Ax} \sigma_{By} \rangle = \sum_{m_A, m_B} m_A m_B w(\mathbf{e}_x, m_A; \mathbf{e}_y, m_B)$.

We adapt the Kitagawa–Ueda squeezing condition in the following manner in order to estimate second-order squeezing (see Sec. 5.3 in Ref. 44). Extending the argument given above, we consider the expectation value of the dyad $J_2 J_2$ instead of (J_2) . In general, $(J_2 J_2)$ is not a null tensor. We may, therefore, impose the orthogonality condition $\langle \mathcal{J} \rangle = 0$, where

$$\mathcal{J} = \frac{1}{2}(\mathbf{v}_1 \cdot J_2 J_2 \cdot \mathbf{v}_2 + \mathbf{v}_2 \cdot J_2 J_2 \cdot \mathbf{v}_1). \quad (26)$$

\mathbf{v}_1 and \mathbf{v}_2 are analogous to the vector \mathbf{v}_\perp in the previous case. The symmetrization with respect to \mathbf{v}_1 and \mathbf{v}_2 in Eq. (26) ensures that \mathcal{J} is real. We consider a set of several different pairs $(\mathbf{v}_1, \mathbf{v}_2)$ for which $\langle \mathcal{J}(t) \rangle = 0$. For each such pair, the variance $(\Delta \mathcal{J})^2$ has been computed, and from this, the minimum variance $(\Delta \mathcal{J}_{\min})^2$ has been obtained. The reference value ($= 0.125$) below which the state is second-order squeezed is obtained by minimizing the corresponding variance for the spin coherent state with respect to θ and ϕ .

V. NMR EXPERIMENT I

We now proceed to examine the NMR experiment I. We will first assess the squeezing properties of the spin system, quantify entanglement with different tomographic entanglement indicators, and comment on the similarities in the dynamics of spin squeezing and entanglement (see Sec. 5.3 in Ref. 44). We also examine the performance of the entanglement indicators in comparison with ξ_{QMI} and negativity. As mentioned in Sec. I, the system of interest comprises ^1H spins (subsystem A), ^{19}F spins (subsystem B), and ^{13}C spins (subsystem M), evolving in time.

Experimentally, such a system was realized using the liquid-state Nuclear Magnetic Resonance (NMR) spectroscopy of ^{13}C , ^1H , and ^{19}F nuclei in the DBFM molecule. The liquid sample consisted of an ensemble of around 10^{15} mutually non-interacting DBFM molecules dissolved in deuterated acetone, placed inside a 11.74 T superconducting magnet. All experiments were performed at ambient temperatures. The nuclear spins interact with the external field via Zeeman interaction, which lifts the degeneracy between spin energy levels. Further, inter-molecular interactions are present, but in the liquid state, these interactions are all averaged out, and only the intra-molecular interactions mediated via covalent bonds survive.⁴⁵ The Hamiltonian of the system in a frame rotating about the quantization axis with respective Larmor frequencies can be written (in units of \hbar) as

$$H_I = \frac{1}{2} \pi (J_{AM} \sigma_{Az} \otimes \sigma_{Mz} + J_{BM} \sigma_{Bz} \otimes \sigma_{Mz} + J_{AB} \sigma_{Az} \otimes \sigma_{Bz}), \quad (27)$$

where the coupling constants $\{J\}$ are as indicated in Fig. 2(a). The interaction between the nuclei along with radio-frequency (RF) pulses can be used to realize the effective Hamiltonian,

$$H_S = 4\chi_S (\sigma_{Ax} + \sigma_{Bx}) \sigma_{Mx}, \quad (28)$$

where χ_S is a constant.³¹ Thus, in each DBFM molecule, the focus is on a chain of three qubits, in the linear topology A–M–B, such

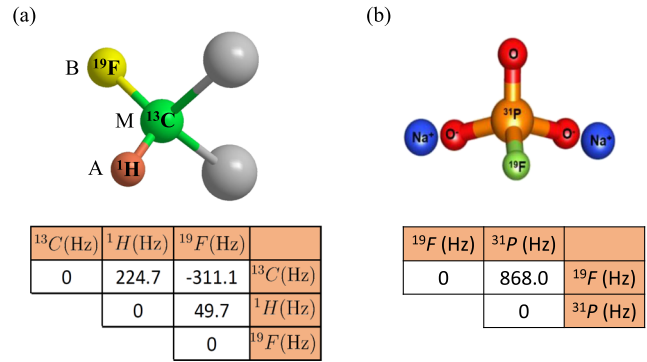


FIG. 2. Spin systems. (a) DBFM molecule and its Hamiltonian parameters forming the three-qubit register used in NMR experiments I and III. (b) NaFP molecule and its Hamiltonian parameters forming the two-qubit register used in NMR experiment II. The off-diagonal elements in each table show the scalar J-coupling values.

that the probe qubits A and B interact with each other only via the mediator qubit M. The three qubit system is then prepared in the initial state given by the density matrix,

$$\rho_{\text{MAB}}(0) = \frac{1}{2} |\phi_+\rangle_{\text{AB}} \langle \phi_+| \otimes \rho_{\text{M}+} + \frac{1}{2} |\psi_+\rangle_{\text{AB}} \langle \psi_+| \otimes \rho_{\text{M}-}, \quad (29)$$

where

$$\rho_{\text{M}+} = |+\rangle_{\text{MM}} \langle +|, \quad \rho_{\text{M}-} = |-\rangle_{\text{MM}} \langle -|,$$

and

$$\left. \begin{aligned} |\psi_+\rangle_{\text{AB}} &= (|\downarrow\rangle_{\text{A}} \otimes |\downarrow\rangle_{\text{B}} + |\uparrow\rangle_{\text{A}} \otimes |\uparrow\rangle_{\text{B}}) / \sqrt{2}, \\ |\phi_+\rangle_{\text{AB}} &= (|\downarrow\rangle_{\text{A}} \otimes |\uparrow\rangle_{\text{B}} + |\uparrow\rangle_{\text{A}} \otimes |\downarrow\rangle_{\text{B}}) / \sqrt{2}. \end{aligned} \right\} \quad (30)$$

Here, $|\uparrow\rangle$ and $|\downarrow\rangle$ denote the eigenstates of σ_z , while $|+\rangle$ and $|-\rangle$ denote those of σ_x . It is straightforward to show that

$$\rho_{\text{MAB}}(t) = \frac{1}{2} |\Psi_0\rangle \langle \Psi_0| + \frac{1}{2} |\Psi_1\rangle \langle \Psi_1|, \quad (31)$$

where

$$\left. \begin{aligned} |\Psi_0\rangle &= |+\rangle_{\text{M}} [\cos(2\chi_S t) |\phi_+\rangle_{\text{AB}} - i \sin(2\chi_S t) |\psi_+\rangle_{\text{AB}}], \\ |\Psi_1\rangle &= |-\rangle_{\text{M}} [\cos(2\chi_S t) |\psi_+\rangle_{\text{AB}} + i \sin(2\chi_S t) |\phi_+\rangle_{\text{AB}}]. \end{aligned} \right\} \quad (32)$$

Of direct relevance to us is the reduced density matrix

$$\rho_{\text{AB}}(t) = \text{Tr}_{\text{M}}(\rho_{\text{MAB}}(t)) \quad (33)$$

corresponding to subsystem AB.

Here, and in the other two experiments reported in Sec. VI, we have carried out the following procedure. (a) We have used the experimentally-obtained tomograms and computed numerical values of the extents of entanglement and squeezing directly, at different instants of time. (b) At these instants, we have numerically obtained the density matrices using the Liouville equation, with the initial state and the Hamiltonian as inputs, and recreated the corresponding tomograms. From the latter, we have computed the extent of entanglement and squeezing. This approach gives us an estimate of the experimental losses. (c) Furthermore, direct computation of

the standard entanglement measures (ξ_{SVNE} , ξ_{QMI}) from both the reconstructed and numerically-obtained density matrices has been carried out. This facilitates assessment of the efficacy of calculations performed with tomograms without resorting to density matrices. Since the focus in this paper is to assess the advantages of the tomographic approach vis-a-vis the density matrix approach, we have used the experimentally-obtained tomogram discounting the error bars. This suffices for our purpose.

Before proceeding further, it is important to point out that, in all these experiments, due to the smallness of the Hilbert space, the relevant density matrices have been easily reconstructed from the tomograms through a two-step procedure. The deviation matrix is first reconstructed from the tomogram, and subsequently, the density matrix is readily computed from the deviation matrix. This procedure is given in Ref. 31. With the increase in the dimension of the Hilbert space, this program is not straightforward and, in fact, poses several challenges as mentioned in Sec. I. In this paper, we have verified that the entanglement indicators obtained solely from tomograms are in good agreement with that computed from reconstructed density matrices. This result, therefore, establishes that the tomographic approach is a powerful alternative in estimating nonclassical effects. By extrapolation, it is evident that this approach is potentially very useful for systems with large Hilbert spaces, be they an array of interacting qubits or coupled CV systems.

We now proceed to examine the spin squeezing properties, and as a first step, we compute the mean spin direction $\mathbf{v}_s(t)$ in NMR experiment I. Since $\langle\sigma_{ix}(t)\rangle$, $\langle\sigma_{iy}(t)\rangle$, and $\langle\sigma_{iz}(t)\rangle$ ($i = A, B$) are all equal to zero, consequently, $\mathbf{v}_s(t)$ is a null vector. Hence, any unit vector \mathbf{v}_\perp can be chosen to obtain the required variance. We have calculated the variance $(\Delta \mathbf{J}_2 \cdot \mathbf{v}_\perp)^2 = \langle(\mathbf{J}_2 \cdot \mathbf{v}_\perp)^2\rangle$ as a function of t for 800 different vectors \mathbf{v}_\perp at each instant. From this, we have identified the minimum variance $(\Delta \mathcal{J}_{\min})^2$ and plotted it as a function of time [Fig. 3(a)]. From the figure, it is evident that the variance obtained numerically using Eq. (33) and that obtained from the experimentally reconstructed density matrices are in good agreement. We also point out that the extent of squeezing, $[1 - 2(\Delta \mathcal{J}_{\min})^2]$, increases with time. We have also verified that the variances obtained from the tomograms agree with those computed from the corresponding density matrix.

In order to estimate second-order squeezing using the procedure given in Sec. IV, we first compute $\langle\mathcal{J}(t)\rangle$. Using Eq. (33), we get

$$\langle\mathcal{J}(t)\rangle = \text{Tr}(\rho_{AB}(t)\mathcal{J}) = \mathbf{v}_{1x}\mathbf{v}_{2x} + \frac{1}{2}\{\mathbf{v}_{1y}\mathbf{v}_{2y} + \mathbf{v}_{1z}\mathbf{v}_{2z} + \sin(4\chi_s t)(\mathbf{v}_{1y}\mathbf{v}_{2z} + \mathbf{v}_{2y}\mathbf{v}_{1z})\}, \quad (34)$$

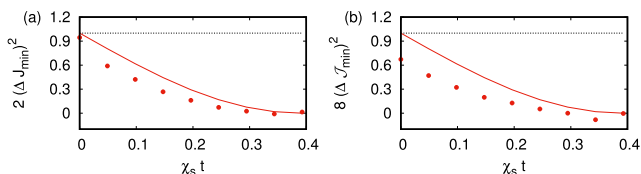


FIG. 3. (a) $2(\Delta \mathcal{J}_{\min})^2$ and (b) $8(\Delta \mathcal{J}_{\min})^2$ vs scaled time $\chi_s t$. The solid curves are computed using Eq. (33) and the dotted curves from experimental data. The black horizontal line in (a) and (b) sets the limit below which the state is squeezed.

where the subscripts x , y , and z denote the corresponding components of \mathbf{v}_1 and \mathbf{v}_2 . {The symmetry between the y and z components in Eq. (34) follows from the fact that $[\sigma_{Ax}\sigma_{Bx}, \rho_{AB}(t)] = 0$.} We have considered a set of 320 different pairs $(\mathbf{v}_1, \mathbf{v}_2)$ for which $\langle\mathcal{J}(t)\rangle = 0$. For each such pair, the variance $(\Delta \mathcal{J})^2$ has been computed, and from this, the minimum variance $(\Delta \mathcal{J}_{\min})^2$ has been obtained. Plots of $(\Delta \mathcal{J}_{\min})^2$ vs t obtained both from the experimentally reconstructed density matrices and from Eq. (33) are shown in Fig. 3(b). The two curves are in reasonable agreement with each other. We note here that the agreement between the two curves increases with time. This can be seen as a reduction in the errors due to statistical techniques adopted in state reconstruction because of the following reason. Here, the magnitude of the off-diagonal elements in the density matrix decreases with time, and, therefore, the tomograms that capture only the diagonal elements become “truer” representations of the corresponding states. There is a consequent reduction in the error, and this is reflected in better agreement between the variances computed from the reconstructed density matrices and that from the theoretical prediction. As in the earlier case, the measure of second-order squeezing, $[1 - 8(\Delta \mathcal{J}_{\min})^2]$, increases with time. We have verified that neither the state of subsystem A nor that of B displays entropic squeezing⁴⁶ at any time.

We turn now to the entanglement dynamics in NMR experiment I. We have computed ξ_{TEI} , ξ_{IPR} , ξ_{BD} , and ξ_{PCC} , and compared with two standard indicators, ξ_{QMI} and the negativity $N(\rho_{AB})$ (negativity has been computed from density matrices in the experiment,³¹ without using the tomographic approach). Negativity is defined as $N(\rho_{AB}) = \frac{1}{2}\sum_i(|\mathcal{L}_i| - \mathcal{L}_i)$. Here, $\{\mathcal{L}_i\}$ is the set of eigenvalues of $\rho_{AB}^{T_A}$, the partial transpose of ρ_{AB} with respect to the subsystem A. (Equivalently, the partial transpose $\rho_{AB}^{T_B}$ may be used.) We find that ξ_{TEI} , ξ_{QMI} , and $N(\rho_{AB})$ are in agreement in their gross features [Fig. 4(a)], with ξ_{TEI} closer to ξ_{QMI} due to the similarity in their definitions. The indicators ξ_{BD} and ξ_{IPR} behave in a manner similar to ξ_{TEI} [Figs. 4(b) and 4(c)]. Surprisingly, the indicator ξ_{PCC} that captures only linear correlations performs well and agrees reasonably well with $N(\rho_{AB})$ [Fig. 4(d)]. This is in contrast to earlier results on bipartite CV and multipartite HQ systems,³⁰ where it was shown that ξ_{PCC} does not reliably track the extent of entanglement. Agreement between the two curves corresponding to the experimental data and the

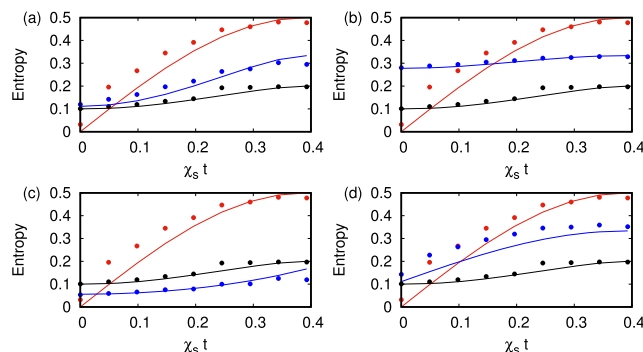


FIG. 4. $N(\rho_{AB})$ (red), $0.1\xi_{\text{QMI}}$ (black), and (a) ξ_{TEI} (blue), (b) ξ_{IPR} (blue), (c) ξ_{BD} (blue), (d) ξ_{PCC} (blue) vs scaled time $\chi_s t$. The solid curves are computed using Eq. (33) and the dotted curves are from experimental data.

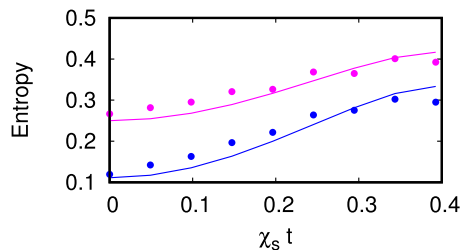


FIG. 5. ξ_{TEI} computed from nine tomographic slices (blue) and ξ'_{TEI} computed from six tomographic slices (magenta) vs scaled time $\chi_s t$. The solid curves are computed using Eq. (33) and the dotted curves are from experimental data.

theoretical prediction follows a trend similar to that pointed out in Fig. 3. The inferences drawn earlier in this context hold true here too. However, the extent of deviation at initial time is comparatively smaller as these indicators are computed directly from the tomograms. This emphasizes the advantages in adopting the tomographic approach.

Typically, our computations involve tomograms obtained over nine basis sets, namely, xx , xy , xz , yx , yy , yz , zx , zy , and zz . To estimate the extent of squeezing, we require all nine “tomographic slices” corresponding to these nine basis sets, as is evident from our procedure to compute $2(\Delta\mathcal{J}_{\min})^2$ and $8(\Delta\mathcal{J}'_{\min})^2$ in Sec. IV. However, a natural question that arises is whether the behavior of the entanglement indicators can be captured from a smaller number of tomographic slices. In NMR experiment I in Fig. 5, we compare ξ_{TEI} obtained using the original nine slices with ξ'_{TEI} , which is a similar averaged indicator computed with only six slices (namely, xx , xy , xz , yx , yy , and yz). With this choice of the reduced number of slices, we see from Fig. 5 that ξ_{TEI} and ξ'_{TEI} are in good agreement with each other. We have verified that this does not hold for other indicators such as ξ_{IPR} . A naive extrapolation of our results would imply that for the bipartite system in NMR experiment II, too, a smaller number of tomographic slices would suffice. However, as shown in Sec. VI, that is not possible.

Returning to the problem at hand, Figs. 6(a) and 6(b) facilitate comparison between $[1 - 2(\Delta\mathcal{J}_{\min})^2]$, $[1 - 8(\Delta\mathcal{J}'_{\min})^2]$, $N(\rho_{\text{AB}})$, ξ_{TEI} , and ξ_{QMI} . It is clear that $N(\rho_{\text{AB}})$ characterizes the degree of squeezing and higher-order squeezing extremely well. ξ_{TEI} and ξ_{QMI} are approximate estimators of squeezing properties. However, we see from Figs. 7(a) and 7(b) that ξ_{PCC} compares well with $[1 - 2(\Delta\mathcal{J}_{\min})^2]$, $[1 - 8(\Delta\mathcal{J}'_{\min})^2]$, and $N(\rho_{\text{AB}})$. The variances and

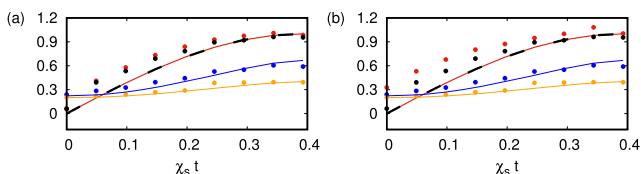


FIG. 6. $2N(\rho_{\text{AB}})$ (black), $2\xi_{\text{TEI}}$ (blue), $0.2\xi_{\text{QMI}}$ (orange), and (a) $[1 - 2(\Delta\mathcal{J}_{\min})^2]$ (red) and (b) $[1 - 8(\Delta\mathcal{J}'_{\min})^2]$ (red) vs scaled time $\chi_s t$. The solid curves are computed using Eq. (33) and the dotted curves are from experimental data.

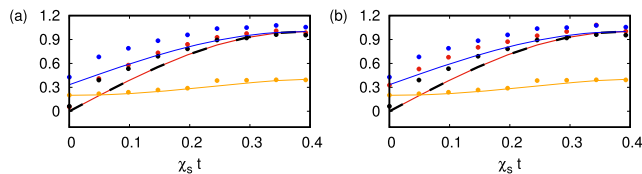


FIG. 7. $2N(\rho_{\text{AB}})$ (black), $3\xi_{\text{PCC}}$ (blue), $0.2\xi_{\text{QMI}}$ (orange), and (a) $[1 - 2(\Delta\mathcal{J}_{\min})^2]$ (red) and (b) $[1 - 8(\Delta\mathcal{J}'_{\min})^2]$ (red) vs scaled time $\chi_s t$. The solid curves are computed using Eq. (33) and the dotted curves are from experimental data.

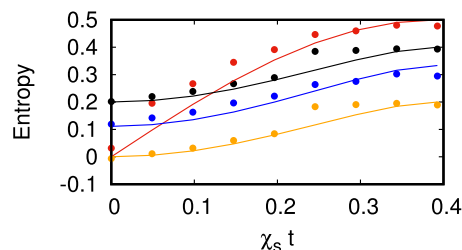


FIG. 8. $N(\rho_{\text{AB}})$ (red), $0.2\xi_{\text{QMI}}$ (black), ξ_{TEI} (blue), and $0.2D(A : B)$ (orange) vs scaled time $\chi_s t$. The solid curves are computed using Eq. (33) and the dotted curves are from experimental data.

covariances seem to capture the behavior of $N(\rho_{\text{AB}})$ quite well, while ξ_{TEI} reflects the behavior of ξ_{QMI} . For completeness, we also present Fig. 8 comparing ξ_{TEI} , ξ_{QMI} , and $N(\rho_{\text{AB}})$ with discord $D(A : B)$. We see that ξ_{TEI} agrees well with both ξ_{QMI} and $D(A : B)$. Our calculations also reveal that ξ_{PCC} is not in good agreement with discord. We highlight here that entanglement dynamics captured by two standard entanglement measures, such as negativity and discord, do not share completely identical trends. So, even the current efficacy of these tomographic indicators is both interesting and useful. Equivalent circuits corresponding to subsystem AB of this NMR experiment at various instants of time have been processed through the IBM Q platform.³³ The entanglement indicators have been obtained through this exercise. The details are reported in the Appendix.

VI. BLOCKADE AND FREEZING IN NUCLEAR SPINS

We now proceed to investigate NMR experiments II and III. As mentioned in Sec. I, the systems of interest in this case comprise N spin qubits ($N = 2$ for II and $N = 3$ for III) and are examined using NMR spectroscopic techniques as they evolve in time. In both cases, the extent of bipartite entanglement has been reported, using discord as the entanglement indicator. In NMR experiment II, each qubit is a subsystem, and in experiment III, one subsystem comprises two qubits and the other has a single qubit. The effective Hamiltonian for N qubits is

$$H_N = \sum_{i=1}^N (\omega_i \sigma_{ix} - \Omega_i \sigma_{iz}) + \sum_{i=1}^{N-1} \sum_{j=i+1}^N \lambda_{ij} \sigma_{iz} \sigma_{jz}, \quad (35)$$

where ω_i , Ω_i , and λ_{ij} are constants, σ_x and σ_z are the usual spin matrices, and the subscripts i, j label the corresponding qubits.

The density matrix at time $t = 0$ is

$$\rho_N(0) = \left(\frac{1-\epsilon}{2^N}\right)\mathbb{I}_N + \epsilon|\psi\rangle\langle\psi|, \quad (36)$$

where \mathbb{I}_N is the identity operator of dimension $2^N \times 2^N$, $|\psi\rangle = |\downarrow\rangle^{\otimes N}$, and ϵ is the purity of the state. Therefore, in principle, $\text{Tr}[\rho_N^2]$ lies between the values 1 (when $\epsilon = 1$) and $1/2^N$ (when $\epsilon = 0$). The time-evolved state is obtained numerically. We compute ξ_{TEI} , ξ_{IPR} , and ξ_{BD} for both the systems from the corresponding tomograms and examine the extent to which they capture the entanglement features seen in the discord as a function of time. We also comment on the spin squeezing properties.

A. NMR experiment II

As mentioned in Sec. I, the experiment has been performed on two nuclear spins using ^{19}F and ^{31}P spins in NaFP [Fig. 2(b)]. Here, ^{19}F and ^{31}P are subsystems 1 and 2, respectively. The internal Hamiltonian for the two qubit system in a doubly rotating frame in the absence of any RF drive is given by

$$H_{\text{ii}} = -\sum_{i=1}^2 \Omega_i \sigma_{iz} + \frac{1}{2} \pi (J_{\text{FP}} \sigma_{1z} \otimes \sigma_{2z}), \quad (37)$$

where J_{FP} is the scalar coupling constant. In order to realize blockade and freezing phenomena, the system is further driven by RF pulses along the x -axis. The effective Hamiltonian is then given by

$$H'_{\text{ii}} = \sum_{i=1}^2 \omega_i \sigma_{ix} + H_{\text{ii}}, \quad (38)$$

where ω_i are the corresponding drive amplitudes. The constants ω_i , Ω_i and $\pi J_{\text{FP}}/2$ in Eq. (38) can be directly mapped to the constants ω_i , Ω_i and λ_{ij} , respectively, in Eq. (35). The system is prepared in a pseudo-pure state, as defined in Eq. (36) with $N = 2$, which is isomorphic to the pure state $|\downarrow\rangle^{\otimes 2}$. Corresponding to this initial state, the discord has been computed for $N = 2$ as a function of time and reported for $\lambda_{12}/(2\pi) = 868$ Hz and $\Omega_1 = \Omega_2 = \lambda_{12}/2$. Three cases have been examined, namely, (i) $\omega_1/(2\pi) = 217$ Hz, $\omega_2 = \omega_1$ (which describes the blockade condition), (ii) $\omega_2/(2\pi) = 217$ Hz, $\omega_1 = \omega_2/4$, and (iii) $\omega_1/(2\pi) = 217$ Hz, $\omega_2 = \omega_1/4$ (which describe

freezing as detailed in Ref. 32). Following a similar procedure, we have now computed ξ_{QMI} as a function of time. This indicator has been obtained both from numerical computations and from the experimentally reconstructed density matrices. In order to examine the performance of the tomographic indicators, we have used the tomograms corresponding to both these density matrices at each instant of time. From these, the corresponding ξ_{TEI} , ξ_{IPR} , and ξ_{BD} are computed.

At each instant considered, the extent of spin squeezing $[1 - 2(\Delta J_{\text{min}})^2]$ is computed using the procedure described in Sec. IV. In this case, the mean spin direction $\mathbf{v}_s(t)$ is not a null vector. A set of unit vectors \mathbf{v}_\perp that are orthogonal to $\mathbf{v}_s(t)$ were obtained using a numerical search program. From these, we have computed the variance and plotted $[1 - 2(\Delta J_{\text{min}})^2]$ as a function of time. Figures 9 and 10 compare the indicators ξ_{TEI} , ξ_{IPR} , and ξ_{BD} with the discord, $[1 - 2(\Delta J_{\text{min}})^2]$, and ξ_{QMI} for cases (i) and (ii), respectively. From the plots, we infer that all the numerically simulated tomographic indicators are in good agreement with the discord. In contrast to NMR experiment I, spin squeezing agrees well with the discord in experiment II. Further, the variances computed from the experimentally reconstructed density matrices and the numerically simulated density matrices are in good agreement. Further, the small deviations between the two can be interpreted as arising from errors due to reconstruction as explained in the case of NMR experiment I. However, the tomographic indicators computed from the experiment do not match well with those from numerical simulations. This is especially the case when the purity of the state is very low ($\epsilon = 10^{-4}$) and, consequently, the extent of entanglement is much less than unity. We have also verified that the inferences drawn from case (iii) are identical to that of case (ii).

As was done in the case of NMR experiment I, we have calculated ξ'_{TEI} with different choices of a reduced number of tomographic slices. In contrast to our inference in NMR experiment I, none of the indicators (ξ_{TEI} , ξ_{IPR} , and ξ_{BD}) are effective when computed from a reduced number of tomographic slices. The crucial difference between the two experiments is in the extent of entanglement. Typically, in NMR experiment I, discord is in the range $[0, 1]$, whereas in NMR experiment II, it is considerably less (the typical range is $[0, 10^{-8}]$). It appears, therefore, that ξ'_{TEI} is a reliable entanglement indicator only for sufficiently strong bipartite entanglement.

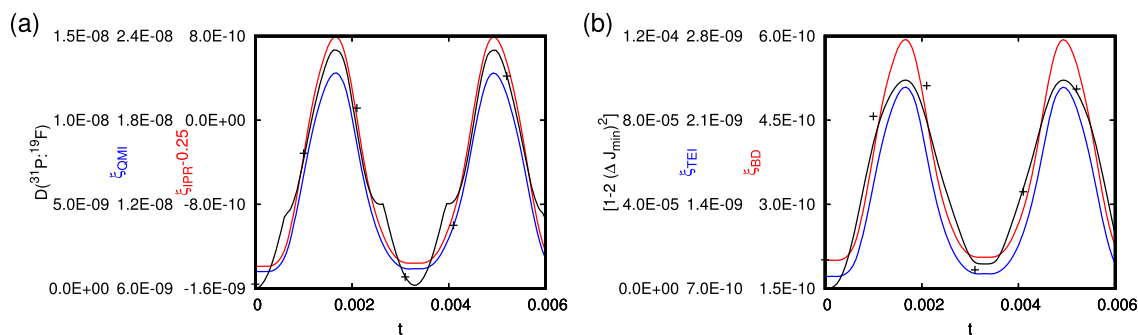


FIG. 9. (a) $D(^{31}\text{P} : ^{19}\text{F})$ (black), ξ_{QMI} (blue), and ξ_{IPR} (red) vs time t in seconds, and (b) $[1 - 2(\Delta J_{\text{min}})^2]$ (black), ξ_{TEI} (blue), and ξ_{BD} (red) vs time t in seconds for case (i). The solid curves are computed by numerical simulation and the crosses are from experimental data.

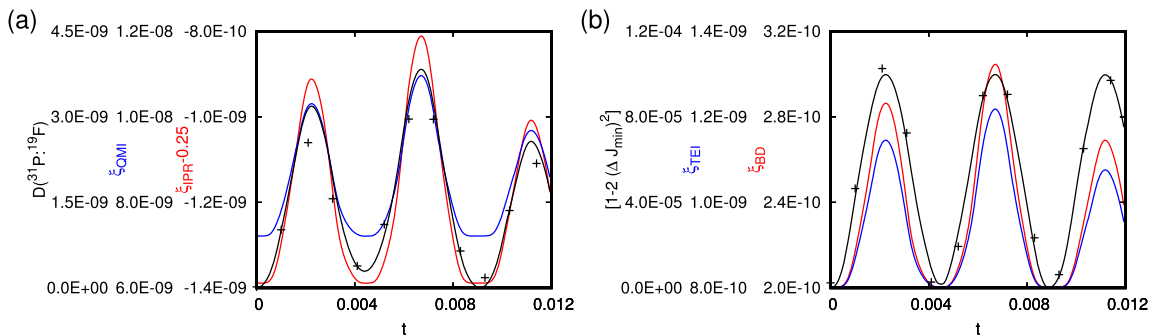


FIG. 10. (a) $D(^{31}\text{P} : ^{19}\text{F})$ (black), ξ_{QMI} (blue), and ξ_{IPR} (red) vs time t in seconds, and (b) $[1 - 2(\Delta J_{\min})^2]$ (black), ξ_{TEI} (blue), and ξ_{BD} (red) vs time t in seconds for case (ii). The solid curves are computed by numerical simulation and the crosses are from experimental data.

We corroborate this below, with further investigations pertaining to NMR experiment III.

B. NMR experiment III

The three qubit experiment has been performed on three nuclear spins by using ^{13}C , ^1H , and ^{19}F spins in DBFM [Fig. 2(a)], the same system as NMR experiment I described in Sec. V. Here, ^{13}C , ^1H , and ^{19}F are subsystems 1, 2, and 3, respectively. The Hamiltonian of the system is of the form

$$H_{\text{iii}} = \sum_{i=1}^3 \omega_i \sigma_{ix} - \sum_{i=1}^3 \Omega_i \sigma_{iz} + H_1, \quad (39)$$

where H_1 is as defined in Eq. (27) (rewritten in terms of subscripts 1, 2, and 3 instead of M, A, and B, respectively). It can be seen that Eq. (39) can be obtained by re-writing Eq. (35) appropriately. The initial density matrix given in Eq. (36) was numerically evolved in time under the Hamiltonian given by Eq. (35) for $N = 3$, and the discord was computed as a function of time,³² for $\lambda_{12}/(2\pi) = 224.7$ Hz, $\lambda_{13}/(2\pi) = -311.1$ Hz, $\lambda_{23}/(2\pi) = 49.7$ Hz, $\Omega_1 = (\lambda_{12} + \lambda_{13})/2$, $\Omega_2 = (\lambda_{12} + \lambda_{23})/2$, and $\Omega_3 = (\lambda_{13} + \lambda_{23})/2$. Four cases have been examined, namely, (A) $\omega_1/(2\pi) = 10$ Hz, $\omega_1 = \omega_2 = \omega_3$ [bipartite entanglement between subsystems (1) and (2, 3)], (B) $\omega_1/(2\pi) = 50$ Hz, $\omega_1 = 5\omega_2 = 5\omega_3$ [bipartite entanglement between

subsystems (1) and (2, 3)], (C) $\omega_2/(2\pi) = 50$ Hz, $\omega_2 = 5\omega_1 = 5\omega_3$ [bipartite entanglement between subsystems (2) and (1, 3)], and (D) $\omega_1/(2\pi) = 50$ Hz, $\omega_1 = \omega_2 = 5\omega_3$ [bipartite entanglement between subsystems (1, 2) and (3)]. Using a similar procedure, we have now computed the corresponding ξ_{QMI} . The tomographic indicators ξ_{TEI} , ξ_{IPR} , and ξ_{BD} and spin squeezing $[1 - (4/3)(\Delta J_{\min})^2]$ were computed, as before. In this case, the spin operator

$$J_3 = (\sigma_{1x} + \sigma_{2x} + \sigma_{3x})\mathbf{e}_x + (\sigma_{1y} + \sigma_{2y} + \sigma_{3y})\mathbf{e}_y + (\sigma_{1z} + \sigma_{2z} + \sigma_{3z})\mathbf{e}_z$$

is used instead of J_2 defined in Eq. (24). Here, $(\Delta J_{\min})^2 < 0.75$ implies spin squeezing.

We have verified that the plots pertaining to cases (A) and (B) are similar to the corresponding plots in Figs. 9 and 10, respectively. As in NMR experiments I and II, in cases (A) and (B) of experiment III, the gross features of entanglement are captured by the indicators. In contrast to experiment I, and similar to experiment II, spin squeezing agrees with discord in cases (A) and (B). The latter, when computed from the experimentally reconstructed density matrices and from numerical simulations, agrees well with each other.

Figures 11 and 12 compare the indicators ξ_{TEI} , ξ_{IPR} , and ξ_{BD} with the discord, $[1 - (4/3)(\Delta J_{\min})^2]$, and ξ_{QMI} for cases (C) and (D), respectively. In case (C), all tomographic indicators agree with

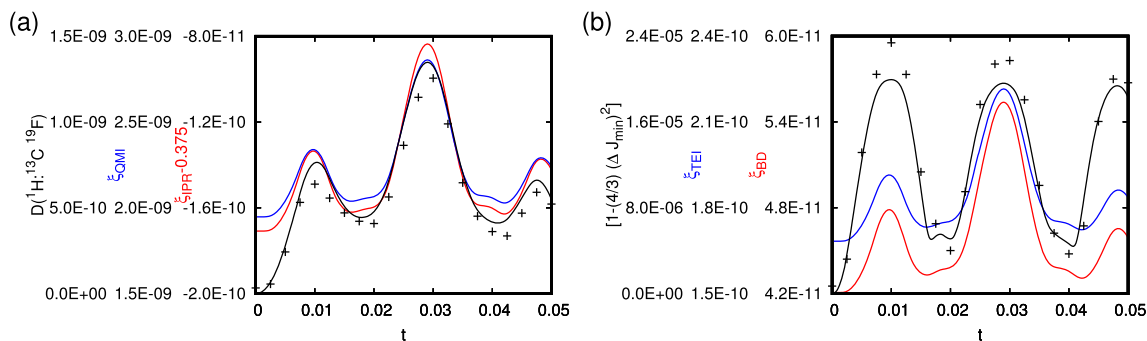


FIG. 11. (a) $D(^1\text{H} : ^{13}\text{C}^{19}\text{F})$ (black), ξ_{QMI} (blue), and ξ_{IPR} (red) vs time t in seconds and (b) $[1 - (4/3)(\Delta J_{\min})^2]$ (black), ξ_{TEI} (blue), and ξ_{BD} (red) vs time t in seconds for case (C). The solid curves are computed by numerical simulation and the crosses are from experimental data.

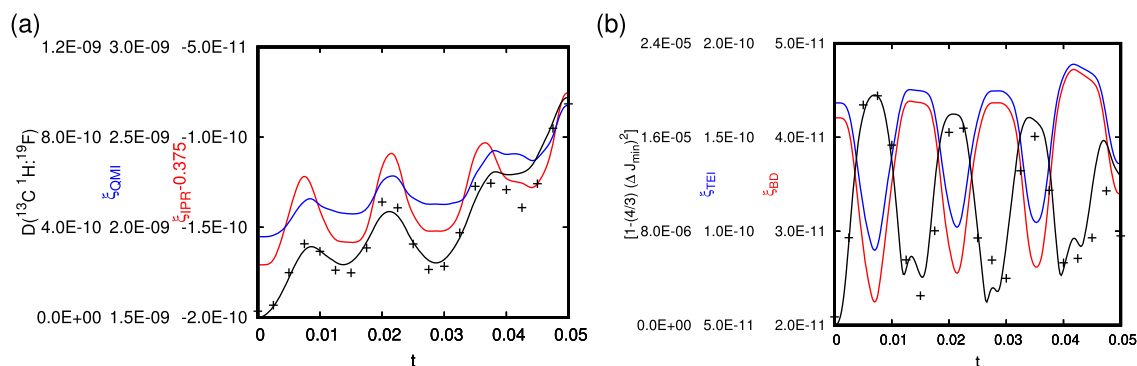


FIG. 12. (a) $D(^{13}\text{C}^1\text{H} : ^{19}\text{F})$ (black), ξ_{QMI} (blue), and ξ_{IPR} (red) vs time t in seconds and (b) $[1 - (4/3)(\Delta J_{\text{min}})^2]$ (black), ξ_{TEI} (blue), and ξ_{BD} (red) vs time t in seconds for case (D). The solid curves are computed by numerical simulation and the crosses are from experimental data.

the discord as before. However, as in experiment I, and in contrast with the other cases that have been examined until now, $[1 - (4/3)(\Delta J_{\text{min}})^2]$ does not mimic the discord effectively.

The inferences in case (D) are in stark contrast to those obtained until now. The unanticipated result is that ξ_{TEI} , ξ_{BD} , and spin squeezing do not mirror the temporal behavior of the discord well. Only ξ_{IPR} agrees reasonably well with the discord.

We note that, as in NMR experiment II, here too the bipartite entanglement is weak, and reducing the number of tomographic slices is not effective. We emphasize that the plots in Figs. 11 and 12 have been obtained retaining all the 27 tomographic slices.

VII. DISCUSSION AND CONCLUSION

Earlier work³⁰ indicates that ξ_{PCC} , which captures linear correlations between the respective quadratures of the two subsystems, does not reliably reflect the extent of entanglement. In direct contrast to this, in NMR experiment I where the state considered is a *mixed* bipartite state, ξ_{PCC} is in good agreement with spin squeezing and negativity $N(\rho_{\text{AB}})$, although not with the discord. Results from both the NMR experiments I and II indicate that all other tomographic entanglement indicators are in good agreement with the discord. We note that NMR experiment II deals with blockade and freezing of spins. We have further shown that novel features could arise in this regard when a tripartite system is partitioned into two subsystems and bipartite entanglement examined, as is revealed by case (D) of NMR experiment III. Thus, the performance of entanglement indicators and the extent to which these indicators and spin squeezing track the discord during dynamical evolution of multipartite systems are very sensitive to the precise manner in which the full system is partitioned into subsystems, as well as to features such as blockade and spin freezing.

Our investigations on these three systems provide some preliminary pointers on the efficacy of identifying an optimal subset of tomographic slices for the computation of the corresponding bipartite entanglement indicator ξ'_{TEI} . If the entanglement is sufficiently strong (NMR experiment I), a subset of tomographic slices suffice. For the experiment, this would indicate a corresponding reduced

number of measurements. However, if the entanglement is weak (NMR experiments II and III), the full set of tomographic slices need to be used. A relevant question is whether the closeness of ξ'_{TEI} to ξ_{TEI} implies strong bipartite entanglement. More detailed investigations need to be carried out before this question can be answered.

ACKNOWLEDGMENTS

The work of S.L. and V.B. was supported, in part, by a seed grant from IIT Madras to C-QuICC (Centre for Quantum Information, Communication and Computing) under the IoE-CoE scheme. B.S. acknowledges the UK STFC “Quantum Technologies for Fundamental Physics” program (Grant No. ST/T006404/1) for partial support.

AUTHOR DECLARATIONS

Conflict of Interest

The authors have no conflicts to disclose.

DATA AVAILABILITY

The data that support the findings of this study are available from the corresponding author upon reasonable request.

APPENDIX: EQUIVALENT CIRCUIT FOR NMR EXPERIMENT I

Corresponding to any instant, the equivalent circuit comprises two parts. Without loss of generality, we describe the circuit at instant $\chi_s t = \pi/8$ [Figs. 13(a) and 13(b)]. Here, q_1 , q_2 , and q_3 are the qubits that follow the dynamics of subsystems M, A, and B, respectively, and

$$RX(\theta) = \begin{bmatrix} \cos(\theta/2) & -i \sin(\theta/2) \\ -i \sin(\theta/2) & \cos(\theta/2) \end{bmatrix} \quad (\text{A1})$$

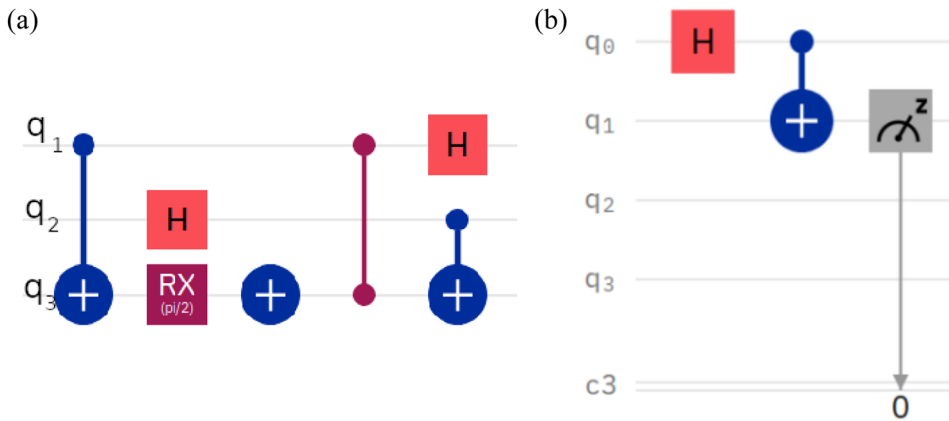


FIG. 13. Parts of the equivalent circuit for NMR experiment I (created using IBM Q). (a) Time evolution and (b) preparation of a maximally mixed state.

with $0 \leq \theta < \pi$. We note that θ is analogous to $4\chi_s t$ in the NMR experiment, and $\chi_s t = \pi/8$ corresponds to $\theta = \pi/2$. The circuit in Fig. 13(a) performs the following task. If the initial state of q_1 , q_2 , and q_3 is set to $|0\rangle$, the final state is analogous to $|\Psi_0\rangle$ [defined in Eq. (32)]. If the initial states of the three qubits are, respectively, $|1\rangle$, $|0\rangle$, and $|0\rangle$, then the output state is analogous to $|\Psi_1\rangle$ [also defined in Eq. (32)].

Thus, by setting the initial state of q_1 to be $\frac{1}{2}(|0\rangle\langle 0| + |1\rangle\langle 1|)$, we can obtain the desired output state analogous to $\rho_{MAB}(t)$. This mixed state is achieved in Fig. 13(b) using an auxiliary qubit q_0 . Tomograms corresponding to $\rho_{AB}(t)$ have been obtained from measurement outcomes on q_2 and q_3 (Fig. 14).

Measurements are taken in the x , y , and z bases corresponding to the matrices defined in Eq. (1). A measurement in the z -basis is

automatically provided by the IBM platform. A measurement in the x -basis is achieved by applying an Hadamard gate followed by a z -basis measurement. Defining the operator

$$S^\dagger = \begin{bmatrix} 1 & 0 \\ 0 & -i \end{bmatrix}, \quad (\text{A2})$$

measurement in the y -basis is achieved by applying S^\dagger , then an Hadamard gate, and finally a measurement in the z -basis. Measurements in the x , y , and z bases are needed for obtaining the spin tomogram in Fig. 15(a) (this is equivalent to the bipartite spin

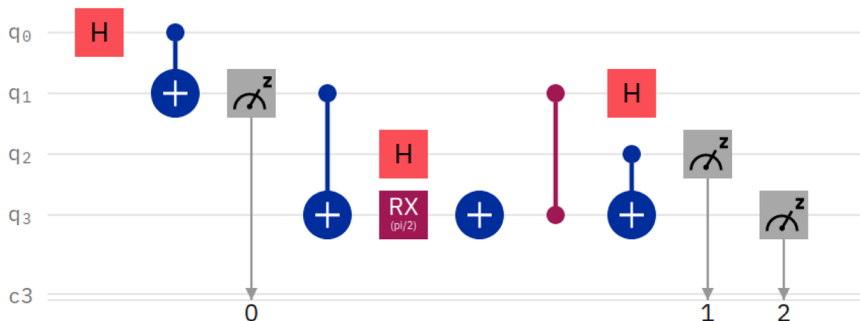


FIG. 14. Equivalent circuit for NMR experiment I (created using IBM Q).

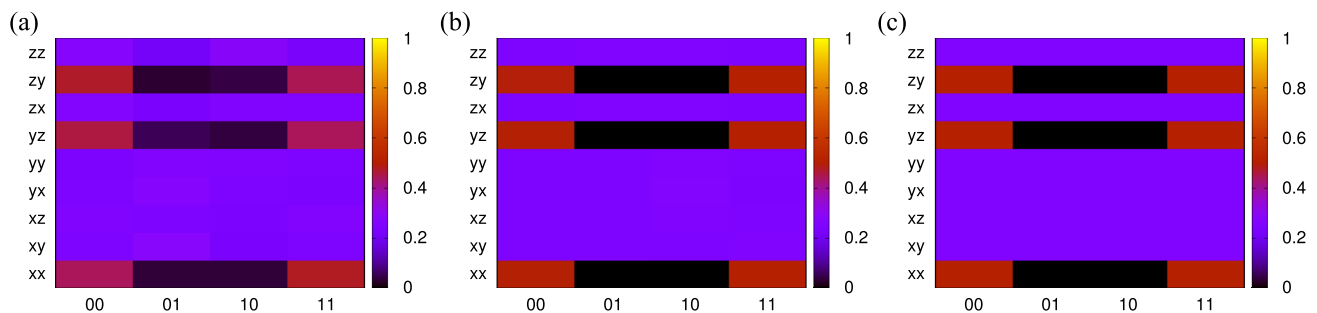


FIG. 15. Tomograms from (a) IBM Q experiment, (b) QASM simulation, and (c) numerical computations of NMR experiment I.

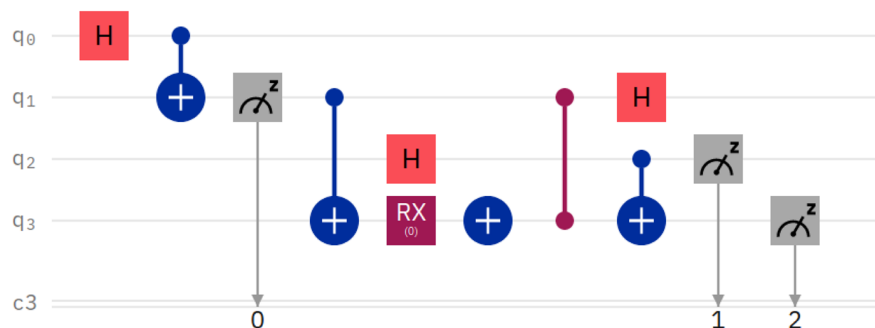


FIG. 16. Equivalent circuit for the initial state analogous to $\rho_{\text{MAB}}(0)$ in NMR experiment I (created using IBM Q).

tomogram in NMR experiment I at $\chi_s t = \pi/8$, in the basis states corresponding to σ_x , σ_y , and σ_z .

In the NMR setup, complete state tomography is possible by rotating the qubits via appropriate unitary transformations and performing measurements in one fixed convenient basis.⁸ Similarly, in the IBM quantum computer, the convenient basis for measurement was the z -basis, as it is the one naturally available in the platform. To measure in any other basis, we resort to rotating the qubit using appropriate gates. Hence, the two measurement processes are comparable.

The spin tomograms have also been obtained experimentally using the IBM superconducting circuit with appropriate Josephson junctions [Fig. 15(a)] and the QASM simulator provided by IBM. The latter does not take into account losses at various stages of the circuit [Fig. 15(b)]. These tomograms have been compared with the numerically generated nuclear spin tomogram where decoherence effects have been neglected [Fig. 15(c)].

Six executions of the experiment were carried out. Each execution of the experiment comprised 8192 runs over each of the nine basis sets. From these six tomograms, ξ_{TEI} has been calculated. The values obtained from the experiment, simulation, and numerical analysis are 0.1941 ± 0.0083 , 0.3334 , and 0.3333 , respectively. The error bar in the experimental value was calculated from the standard deviation of ξ_{TEI} . The experimental value differs from those obtained in the simulation of circuit and the model because of inevitable losses.

The circuit corresponding to the initial state can be obtained by setting θ to zero (Fig. 16). The corresponding values of ξ_{TEI} obtained from the experiment, simulation of the circuit and the model are

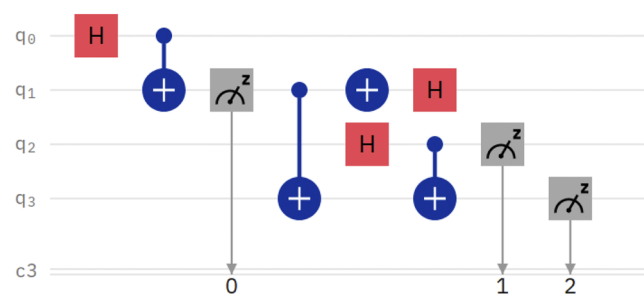


FIG. 17. An alternative equivalent circuit for the initial state analogous to $\rho_{\text{AB}}(0)$ in NMR experiment I (created using IBM Q).

0.0676 ± 0.0065 , 0.1113 , and 0.1111 , respectively. This demonstrates that substantial losses arise even in generating the initial state using this circuit. It is more efficient to construct the initial state circuit in Ref. 31 (Fig. 17) as it involves a smaller number of components.

The values for ξ_{TEI} obtained from the experiment, simulation, and model corresponding to this circuit are 0.0720 ± 0.0025 , 0.1112 , and 0.1111 , respectively. As expected, the experimental value agrees better with the simulation of the circuit and numerical computation of the model.

REFERENCES

- H. Kampermann and W. S. Veeman, *J. Chem. Phys.* **122**, 214108 (2005).
- I. A. Silva, J. G. Filgueiras, R. Aucçaise, A. M. Souza, R. Marx, S. J. Glaser, T. J. Bonagamba, R. S. Sarthour, I. S. Oliveira, and E. R. deAzevedo, "NMR contributions to the study of quantum correlations," in *Lectures on General Quantum Correlations and Their Applications*, edited by F. F. Fanchini, D. d. O. Soares Pinto, and G. Adesso (Springer, Cham, 2017), pp. 517–542.
- W. Scherer and M. Mehring, *J. Chem. Phys.* **128**, 052305 (2008).
- S. Singha Roy and T. S. Mahesh, *J. Magn. Reson.* **206**, 127 (2010).
- M. R. Wasielewski, M. D. E. Forbes, N. L. Frank, K. Kowalski, G. D. Scholes, J. Yuen-Zhou, M. A. Baldo, D. E. Freedman, R. H. Goldsmith, T. Goodson *et al.*, *Nat. Rev. Chem.* **4**, 490 (2020).
- B. K. Rugg, M. D. Krzyaniak, B. T. Phelan, M. A. Ratner, R. M. Young, and M. R. Wasielewski, *Nat. Chem.* **11**, 981 (2019).
- X. Kong, T. Xin, S.-J. Wei, B. Wang, Y. Wang, K. Li, and G.-L. Long, *Quantum Inf. Process.* **17**, 297 (2018).
- L. M. K. Vandersypen and I. L. Chuang, *Rev. Mod. Phys.* **76**, 1037 (2005).
- S. Sinha, J. Emerson, N. Boulant, E. M. Fortunato, T. F. Havel, and D. G. Cory, *Quantum Inf. Process.* **2**, 433 (2003).
- R. Aucçaise, A. G. Araujo-Ferreira, R. S. Sarthour, I. S. Oliveira, T. J. Bonagamba, and I. Roditi, *Phys. Rev. Lett.* **114**, 043604 (2015).
- R. Laflamme, E. Knill, W. H. Zurek, P. Catasti, and S. V. S. Mariappan, *Philos. Trans. R. Soc. London, Ser. A* **356**, 1941 (1998).
- G. Teklemariam, E. M. Fortunato, M. A. Pravia, Y. Sharf, T. F. Havel, D. G. Cory, A. Bhattaharyya, and J. Hou, *Phys. Rev. A* **66**, 012309 (2002).
- J. G. Filgueiras, T. O. Maciel, R. E. Aucçaise, R. O. Vianna, R. S. Sarthour, and I. S. Oliveira, *Quantum Inf. Process.* **11**, 1883 (2012).
- J. Teles, E. R. deAzevedo, R. Aucçaise, R. S. Sarthour, I. S. Oliveira, and T. J. Bonagamba, *J. Chem. Phys.* **126**, 154506 (2007).
- D. Zanuttini, I. Blum, L. Rigutti, F. Vurpillot, J. Douady, E. Jacquet, P.-M. Anglade, and B. Gervais, *J. Chem. Phys.* **147**, 164301 (2017).
- J.-S. Lee, *Phys. Lett. A* **305**, 349 (2002).
- K. Bartkiewicz, A. Černoch, K. Lemr, and A. Miranowicz, *Sci. Rep.* **6**, 19610 (2016).
- S. J. Ginthör, J. Schlagnitweit, M. Bechmann, and N. Müller, *Magn. Reson.* **1**, 165 (2020).
- S. I. Kabanikhin, *J. Inverse Ill-Posed Probl.* **16**, 317 (2008).

- ²⁰Z. Hou, H.-S. Zhong, Y. Tian, D. Dong, B. Qi, L. Li, Y. Wang, F. Nori, G.-Y. Xiang, C.-F. Li, and G.-C. Guo, *New J. Phys.* **18**, 083036 (2016).
- ²¹T. Baumgratz, A. Nüßeler, M. Cramer, and M. B. Plenio, *New J. Phys.* **15**, 125004 (2013).
- ²²J. G. Titchener, M. Gräfe, R. Heilmann, A. S. Solntsev, A. Szameit, and A. A. Sukhorukov, *npj Quantum Inf.* **4**, 19 (2018).
- ²³D. Gross, Y.-K. Liu, S. T. Flammia, S. Becker, and J. Eisert, *Phys. Rev. Lett.* **105**, 150401 (2010).
- ²⁴W.-T. Liu, T. Zhang, J.-Y. Liu, P.-X. Chen, and J.-M. Yuan, *Phys. Rev. Lett.* **108**, 170403 (2012).
- ²⁵A. Steffens, C. A. Riofrío, W. McCutcheon, I. Roth, B. A. Bell, A. McMillan, M. S. Tame, J. G. Rarity, and J. Eisert, *Quantum Sci. Technol.* **2**, 025005 (2017).
- ²⁶X. Chai, Y.-P. Lu, A.-n. Zhang, and Q. Zhao, *Phys. Rev. A* **99**, 042321 (2019).
- ²⁷X. Li, J. Shang, H. K. Ng, and B.-G. Englert, *Phys. Rev. A* **94**, 062112 (2016).
- ²⁸M. Rohith and C. Sudheesh, *J. Opt. Soc. Am. B* **33**, 126 (2016).
- ²⁹B. Sharmila, S. Lakshmibala, and V. Balakrishnan, *Quantum Inf. Process.* **18**, 236 (2019).
- ³⁰B. Sharmila, S. Lakshmibala, and V. Balakrishnan, *J. Phys. B: At., Mol. Opt. Phys.* **53**, 245502 (2020).
- ³¹S. Pal, P. Batra, T. Krisnanda, T. Paterek, and T. S. Mahesh, *Quantum* **5**, 478 (2021).
- ³²V. R. Krithika, S. Pal, R. Nath, and T. S. Mahesh, *Phys. Rev. Res.* **3**, 033035 (2021).
- ³³See <https://quantum-computing.ibm.com/support> for IBM Q: Documentation and support.
- ³⁴See <https://qiskit.org> for Qiskit: An open-source framework for quantum computing.
- ³⁵R. T. Thew, K. Nemoto, A. G. White, and W. J. Munro, *Phys. Rev. A* **66**, 012303 (2002).
- ³⁶L. Viola and W. G. Brown, *J. Phys. A: Math. Theor.* **40**, 8109 (2007).
- ³⁷R. Smith, *Stat* **4**, 291 (2015).
- ³⁸S. Kullback and R. A. Leibler, *Ann. Math. Stat.* **22**, 79 (1951).
- ³⁹T. M. Cover and J. A. Thomas, *Elements of Information Theory* (Wiley-Interscience, Hoboken, 2006).
- ⁴⁰C. Bishop, *Pattern Recognition and Machine Learning* (Springer, New York, 2006).
- ⁴¹T. Kailath, *IEEE Trans. Commun. Technol.* **15**, 52 (1967).
- ⁴²J. Ma, X. Wang, C. P. Sun, and F. Nori, *Phys. Rep.* **509**, 89 (2011).
- ⁴³M. Kitagawa and M. Ueda, *Phys. Rev. A* **47**, 5138 (1993).
- ⁴⁴B. Sharmila, Ph.D. thesis, Indian Institute of Technology Madras, 2020, [arXiv:2009.09798](https://arxiv.org/abs/2009.09798).
- ⁴⁵M. H. Levitt, *Spin Dynamics: Basics of Nuclear Magnetic Resonance* (Wiley, New York, 2001).
- ⁴⁶H. Maassen and J. B. M. Uffink, *Phys. Rev. Lett.* **60**, 1103 (1988).